High-Enthalpy Effects on Hypersonic Boundary-Layer Transition: Experimental and Numerical Comparison

Ahsan Hameed* and Nick J. Parziale†
Stevens Institute of Technology, Hoboken, New Jersey 07030
Joseph Kuehl,‡ Tony Liang,§ and Kevin Graziose¶
University of Delaware, Newark, Delaware 19716
Christoph Brehm** and Sean David Dungan††
University of Maryland, College Park, Maryland 20742
Jean-Philippe Brazier‡‡
ONERA/DMPE, Toulouse University, F-31055 Toulouse, France
and
Laura Paquin§§
North Carolina State University, Raleigh, North Carolina 27606

https://doi.org/10.2514/1.J064456

In this paper, results from two experiments performed at California Institute of Technology's T5 free-piston reflected shock tunnel are compared to numerical stability computations conducted using various stability analysis tools. The goal of this comparison is to begin understanding the range of boundary-layer transition predictability using different stability approaches for high-enthalpy flows. The analysis is focused on the physics of the second-mode instability at high enthalpy and the role of high-temperature effects. Although the stability solvers considering thermochemical nonequilibrium were best at estimating the measured second-mode frequency ($f_{2M} \approx 1250$ kHz for shot 2990, $f_{2M} \approx 1235$ kHz for shot 3019), they overpredicted the most amplified frequency by approximately 16–23%. A moderate spread in the predicted most amplified frequency was also observed between the different solvers. The solvers estimated a most amplified frequency range of approximately 1450–1550 kHz for shot 2990 and approximately 1525–1650 kHz for shot 3019. There was also significant inconsistency observed in predicting the peak N-factor magnitude, ranging from $N = 12.5$–16 for shot 2990 and from $N = 12.3$–19 for shot 3019.

Nomenclature

A	=	disturbance amplitude function
E	=	x-component of total flux vector
F	=	y-component of total flux vector
f_{2M}	=	second-mode peak frequency, kHz
G	=	z-component of total flux vector
h_R	=	reservoir enthalpy, MJ/kg
M_X	=	freestream Mach number
P_R	=	reservoir pressure, MPa
P_X	=	freestream pressure, kPa
R_N	=	cone nose-tip radius, mm
Re	=	Reynolds number
Re_X^U	=	freestream unit Reynolds number, 1/m
T_E	=	boundary-layer edge temperature, K
T_R	=	reservoir temperature, K
T_W	=	wall temperature, K
Tv_X	=	freestream vibrational temperature, K
U_X	=	freestream velocity, m/s
U_e	=	boundary-layer edge velocity, m/s
U_s	=	incident shock speed, m/s
ν_e	=	boundary-layer edge kinematic viscosity, m^2/s
W	=	conservative state (ρ, ρu, ρv, ρw, ρE_t)
y	=	species mass fraction
α	=	streamwise wavenumber, 1/m
δ_r	=	reference boundary-layer length scale, m
δ_{99}	=	boundary-layer thickness, mm
ρ_R	=	reservoir density, kg/m^3
ρ_X	=	freestream density, kg/m^3
ϕ'	=	disturbance field
$\tilde{\phi}$	=	disturbance shape function
ω	=	angular frequency, rad/s

Presented as Paper 2024-0289 at the 2024 AIAA Science and Technology Forum and Exposition, Orlando, FL, January 8–12, 2024.; received 7 June 2024; accepted for publication 5 March 2025; published online 25 April 2025.

*Graduate Student, Mechanical Engineering, 1 Castle Point on Hudson.
†Professor, Mechanical Engineering, 1 Castle Point on Hudson. Associate Fellow AIAA.
‡Associate Professor, Mechanical Engineering, 130 Academy Street.
§Graduate Student, Mechanical Engineering, 130 Academy Street. Student Member AIAA.
¶Graduate Student, Mechanical Engineering, 130 Academy Street. Student Member AIAA.
**Associate Professor, Aerospace Engineering, 3179 Glenn L. Martin Hall Bldg; cbrehm1@umd.edu. Member AIAA.
††Graduate Research Assistant, Aerospace Engineering, 3179 Glenn L. Martin Bldg; sdungan@umd.edu. Student Member AIAA.
‡‡Research Scientist; jean-philippe.brazier@onera.fr.
§§Assistant Professor, Mechanical and Aerospace Engineering, 1840 Entrepreneur Drive. Member AIAA.

I. Introduction

UNDERSTANDING the process of boundary-layer transition at flight-relevant enthalpy is important to hypersonic vehicle design. Following the onset of boundary-layer transition, there is a drastic increase in aeroheating and viscous shear stress experienced by the vehicle. During tests of ballistic reentry vehicles, the surface heating rate was found to have increased by a factor of 5 downstream of the transition location [1]. For slender bodies, the heating rate increased by a factor of 3 following the transition of the laminar boundary layer [2]. Additionally, there remains considerable uncertainty in predicting the location of boundary-layer transition. Reviewers noted a 60% error in estimating the location of transition along the body of the National Aerospace Plane [3], and a review of hypersonic flight data [1] found a 300% uncertainty in transition location prediction. The substantial increase in aeroheating and the large degree of uncertainty associated with predicting the transition location suggest that the process of hypersonic boundary-layer transition is relevant but not well understood.

At the high enthalpies experienced during hypersonic flight, the temperature at the boundary-layer edge (T_E) is greater than the temperature of the vehicle's wall (T_W). In his analysis of Sherman and Nakamura's [4] reentry flight data for a 22° half-angle blunt cone at Mach 6, Malik [5] computed a postshock temperature of 3300 K, giving a wall-to-edge temperature ratio (T_W/T_E) of 0.22. Studies have shown the lower wall-to-edge temperature ratio destabilizes Mack's second-mode instability [6–8]. Through a chemical equilibrium, thermal nonequilibrium LST analysis, Bitter and Shepherd [9] found that decreasing the wall-to-edge temperature ratio to values more representative of conditions in high-enthalpy facilities doubled the maximum second-mode N-factor. The high level of wall cooling was also found to produce unique boundary-layer features. In addition to the near-wall sonic line, which acts as a wave guide and traps the acoustic disturbance waves, when the disturbance phase speed is slow enough, a second supersonic region emerges above the critical layer, with its own relative sonic line [10]. In this region, the disturbance phase speed travels supersonically upstream with respect to the freestream. The solution to the boundary-layer stability equations is wave-like in this region, and the decaying acoustic waves emanating out of the boundary layer are slanted at approximately the Mach wave angle. Bitter and Shepherd's analysis at cooled-wall conditions suggested that these supersonic unstable modes caused the second-mode instability to remain unstable over a broader range of frequencies [9]. Knisely and Zhong further investigated the supersonic mode over a highly cooled (case 1: $T_W/T_E = 0.2$; case 2: $T_W/T_E = 0.667$), 5° blunt cone using linear stability theory (LST) [10] and direct numerical simulation (DNS) [11]. Their work confirmed the existence of the supersonic mode using both DNS and LST for case 1, but they were only able to resolve the weak supersonic mode at the higher temperature ratio using DNS. They also confirmed the destabilizing effects of the cooled wall on the supersonic mode [9,12]. Chuvakhov and Fedorov [12] suggested that the supersonic mode may have stabilizing effects on the second-mode instability by radiating energy away from the boundary layer. Unnikrishnan and Gaitonde [13] investigated the effect of a cooled wall on a Mach 6 boundary layer using a sequence of LST, nonlinear two-dimensional, and three-dimensional DNS. While the cooled wall increased the spontaneous radiation of the acoustic waves out of the boundary layer, they found that the destabilizing effect of the lower wall-to-edge temperature ratio was much stronger and did not observe an attenuation of the second-mode instability.

Additional studies performed at high levels of wall cooling have focused on the effects of chemical reactions. Using parabolized stability equations (PSE) to analyze Mach 20 flow over a sharp, 6° wedge, Chang et al. [14] estimated the transition onset to be at 14 ft for an equilibrium gas model and 39 ft for a perfect gas model, highlighting the importance of accounting for flow chemistry at high enthalpy. Using computational fluid dynamics and linear stability theory, Johnson et al. [15] reproduced the conditions of shock tunnel experiments performed by Adam and Hornung [16] and Germain and Hornung [17] at California Institute of Technology's free-piston shock tunnel, T5. The computational trends agreed with the experimental observations; the transition Reynolds number increased with increasing freestream total enthalpy, with the rate of increase being greater for gases with lower dissociation energies. Generally, chemical reactions were found to produce a more unstable boundary layer. However, the introduction of chemistry was found to stabilize or destabilize the boundary layer depending on the endothermic or exothermic nature of the reaction, with exothermic reactions having higher disturbance amplification rates. Malik [5] confirmed the destabilizing nature of chemistry in his analysis of high-Mach-number transition data using a reacting flow parabolized stability equations code. Despite the large discrepancy in edge conditions and transition Reynolds numbers between the two cases analyzed, the N-factors at the experimentally observed transition onset locations were remarkably similar and compared well with results from hypersonic flight experiments and quiet tunnels.

Due to the practical and physics-related challenges inherent to high-enthalpy ground-test facilities, namely, high cost of construction and operation, short test duration, flow quality, and particulate contamination, few experimental investigations have been performed at flight-relevant enthalpies. Vidal and Golian [18] investigated the heat transferred to catalytic and noncatalytic surfaces on a sharp flat plate in a shock tube at $T_W/T_E = 0.09$. East et al. [19] measured heat-transfer rates over a flat plate in the T3 free-piston reflected shock tunnel at stagnation enthalpies from 2 to 51 MJ/kg. Germain [20] performed an exploratory study at T5 using a 5° half-angle cone and found real-gas effects stabilized the boundary layer. Adam's [21] studies at T5 reinforced Germain's [20] earlier results, noting that the transition Reynolds number increased with increasing reservoir enthalpy. Additional boundary-layer transition and stability research was performed in T5 to test the performance of hypersonic boundary-layer control schemes [22,23], quantify the role of energy exchange between the boundary-layer instability and the fluid [24], and show the increase in the transition Reynolds number of a test gas by seeding its boundary layer with a gas to dampen the acoustic instability [25–29]. Parziale et al. [30–32] and Parziale [33] used a novel, nonintrusive, optical flow-diagnostic technique called focused laser differential interferometry (FLDI) at T5 to track the evolution of the second-mode instability along the model. Knowing the spacing between the FLDI detectors and the time at which the disturbance signal was registered by each probe, Parziale et al. were able to determine the group velocity of the narrowband second-mode disturbance to be nearly equal to the edge velocity of the boundary layer. Additional high-enthalpy experimental campaigns have been performed in shock tunnels around the world. In JAXA's HIEST facility, Tanno et al. [34,35] performed experiments at stagnation enthalpies up to 18 MJ/kg. They used surface-mounted thermocouples to determine the transition Reynolds number over a 7° half-angle cone and were able to measure the second-mode instability using pressure transducers up to a stagnation enthalpy of 12 MJ/kg. Laurence et al. [36] performed low-enthalpy experiments ($h_R = 3.1$–$3.3\ \mathrm{MJ/kg}$) and a single high-enthalpy experiment ($h_R = 11.9\ \mathrm{MJ/kg}$) at DLR's HEG facility. They observed the nature of the wavepacket differed depending on the enthalpy, with the disturbance energy more closely concentrated near the wall for the high-enthalpy condition.

In this work, results from two experiments performed by Hameed et al. [37,38] and Paquin et al. [39] at the T5 free-piston reflected shock tunnel are compared to numerical stability computations conducted using various stability analysis tools: STABL, MAMOUT from ONERA/DMPE, JoKHeR from the University of Delaware, and CHAMPS from the University of Maryland. Both experiments feature highly cooled boundary layers and a blunt cone nose tip. To evaluate the accuracy of the numerical methods, a comparison is made between the experimentally determined frequency of the second-mode instability and the computationally determined most amplified frequency. The analysis is focused on the physics of the second-mode instability at high enthalpy and the role of high-temperature gas effects.

II. Facility and Experimental Setup

A. T5 Reflected Shock Tunnel

The experiments in this campaign were performed at the California Institute of Technology's T5 free-piston reflected shock tunnel (schematically represented in Fig. 1). T5 is capable of producing flows up to a specific reservoir enthalpy of 25 MJ/kg, reservoir pressure of 100 MPa, and reservoir temperature of 10,000 K. By generating high-enthalpy flows at high density, this facility simulates the chemical nonequilibrium effects of vehicles flying at hypervelocity speeds through the atmosphere. Additional information regarding the capabilities of T5 can be found in Hornung [40].

T5 is separated into four sections: secondary reservoir, compression tube, shock tube, and test section. In preparation for an experiment, a thick steel primary diaphragm is installed at the shock

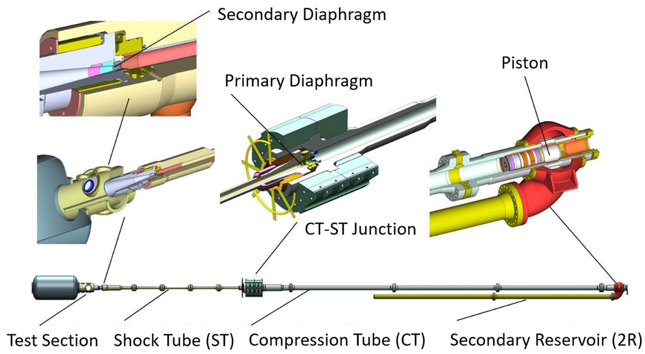

Fig. 1 Schematic of the T5 reflected shock tunnel showing the various sections of the facility.

tube/compression tube junction, a thin Mylar secondary diaphragm is placed between the test section and the shock tube, and a 120 kg piston is loaded in the launch manifold between the secondary reservoir and the compression tube. Next, each section of the facility is independently evacuated to an acceptable level of vacuum. The shock tube is then filled with the test gas (ALPHAGAZ™ air for these experiments), the compression tube is filled with a helium/argon mixture, and the secondary reservoir is pressurized with air. The piston is launched down the compression tube once the pressurized air in the secondary reservoir is allowed to push against the back of the piston. The accelerating piston adiabatically compresses the driver gas in the compression tube until the primary diaphragm is ruptured. The rupture of the primary diaphragm causes a shock wave to propagate into the shock tube, which reflects off the end wall, bursts the secondary diaphragm, and reprocesses the test gas to the nozzle reservoir conditions. The test gas is then expanded through the converging–diverging contoured nozzle to a hypersonic Mach number (typically $M_\infty \approx 5.2$) in the test section.

B. Test Model

A 5° half-angle cone with a slightly blunted interchangeable nose tip ($R_N = 2$ mm) was used as the model for these experiments. The cone was placed at approximately 0° angle of attack in the spanwise center of the test section. Shot 2990 used a cone with no interior cooling capabilities. For shot 3019, an actively cooled cone was manufactured to identical exterior dimensions as the original model. The actively cooled cone was machined in two halves and featured an internal cavity to house a cooling coil and a copper heat exchanger. The cooling coil extended approximately halfway into the cone. Liquid nitrogen (LN_2) entered and exited the coil from the rear of the cone in a single-pass configuration. The copper heat exchanger was installed upstream of the cooling coil and extended the cooling effect toward the cone's leading edge, decreasing its surface temperature in this region. De-icer was applied to the cone's surface to reduce the risk of frost developing during the cooling process. To measure the cone's surface temperature distribution before the experiment, the cone was instrumented with type K thermocouples internally routed toward the cone's surface and located at various circumferential positions longitudinally along the cone. A model of the actively cooled cone is presented as an inset in Fig. 2.

C. Calculation of Run Conditions

The nozzle reservoir conditions were used to estimate the freestream run conditions. The thermodynamic state of the test gas in the nozzle reservoir was determined using the shock tube pressure, P_1, and the measured incident shock speed, U_s. Using Cantera [41] with the Shock and Detonation Toolbox [42], isentropic expansion of this state to the reservoir pressure, P_R, was assumed, accounting for weak expansion or compression waves that are reflected between the contact surface and the shock tube end wall. The calculated nozzle reservoir conditions were input into the University of Minnesota Nozzle Code to determine the freestream conditions at the exit of the contoured nozzle [43–46]. The reservoir and freestream

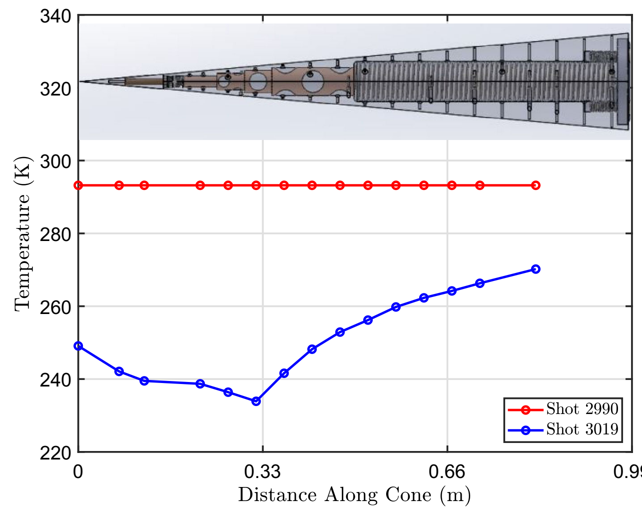

Fig. 2 Temperature distribution along model for shot 2990 and shot 3019. Model of cooled cone shown as inset.

conditions for the shots discussed in this manuscript are presented in Tables 1 and 2. The freestream conditions are chosen to be an areal average of the DPLR output at approximately 580 ± 10 mm, the approximate distance from the nozzle's throat to the location of the model's nose tip. The temperature profile along the cone is shown in Fig. 2. Shot 2990 featured a room-temperature wall. The wall temperature profile varied for shot 3019 and was specified based on thermocouple measurements taken immediately before the run.

D. FLDI Setup

The components utilized to generate the FLDI diagnostic for shot 2990 are shown in Fig. 3. The 532 nm linearly polarized beam output of a Cobolt 05-01 laser was first expanded using a diverging lens. The diverging beam was then passed through two diffractive optics (Holo/Or MS-474-Q-Y-A and DS-192-Q-Y-A) to generate a grid of beams, which was circularly polarized using a quarter-wave plate. Each beam in the grid was split once more into orthogonally polarized beam pairs using a 2 arcminute Wollaston prism. Next, the beams passed through a converging lens and then entered the test section. The position of the diverging lens was adjusted relative to the upbeam converging lens (left C_2 in Fig. 3) to locate the focus of the beams above the top-center of the cone. The lowest row of beams was positioned within the boundary layer, at a height equal to approximately half of the boundary-layer thickness. Downbeam of the test section, the diverging FLDI beam pairs were again focused using a converging lens and then recombined using a Wollaston prism of an equivalent separation angle. Finally, the grid of beams was passed through a linear polarizer, and each beam was steered onto an individual photodiode using an array of lenses.

The FLDI beam pairs used to probe the flow in shot 2990 are shown in Fig. 4, with major and minor tick marks spaced 1 and 0.1 mm apart, respectively. In this experiment, the flow was interrogated using the lowest row and upstream column of beam pairs. This selection positioned two beam pairs within the boundary layer at approximately 0.635 mm above the cone surface (FLDI probes C and D as shown in the figure) and two beam pairs at various heights above the boundary layer (FLDI probes A and B as shown in the figure). The boundary layer, shown as the dashed line in Fig. 4, was determined to be approximately 1 mm thick at the measurement location of 680 mm along the cone. The velocity profile at this position is represented as a solid white line. Both the boundary-layer thickness and the velocity profile were determined using DPLR.

E. Schlieren Setup

The schlieren setup described in Paquin et al. [47] was used for shot 3019. A Cavilux HF laser was used as the light source, with an

Table 1 Reservoir conditions

Shot	Gas	P_R, MPa	h_R, MJ/kg	T_R, K	ρ_R, kg/m^3	y_{N_2}, -	y_{O_2}, -	y_{NO}, -	y_N, -	y_O, -	R_N, mm	Diag, -
2990	Air	59.6	8.86	5727	33.3	0.699	0.068	0.141	0.003	0.090	2	FLDI
3019	Air	61.6	9.67	6076	31.9	0.698	0.052	0.137	0.005	0.108	2	Schlieren

Table 2 Freestream conditions

Shot	U_∞, m/s	ρ_∞, kg/m^3	P_∞, kPa	T_∞, K	Tv_∞, K	M_∞, -	Re^U_∞, 1/m	y_{N_2}, -	y_{O_2}, -	y_{NO}, -	y_N, -	y_O, -
2990	3809	0.087	34.2	1355	1363	5.13	6.35e + 06	0.733	0.187	0.073	0.000	0.007
3019	3953	0.085	37.3	1511	1518	5.03	5.99e + 06	0.733	0.184	0.073	0.000	0.010

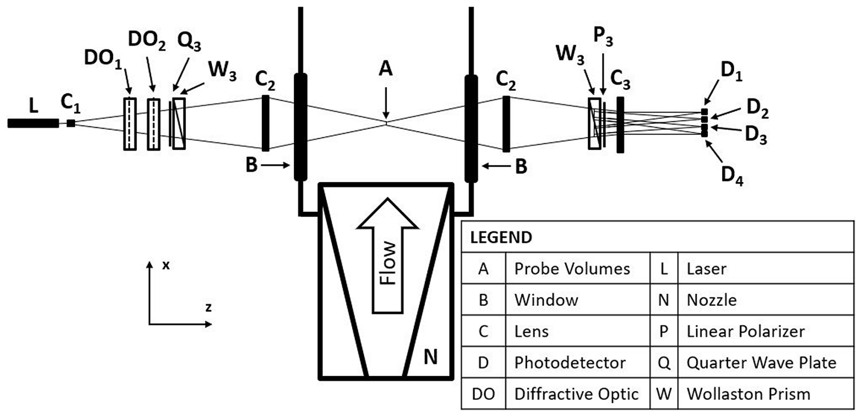

Fig. 3 Optical components used to generate the FLDI diagnostic for shot 2990.

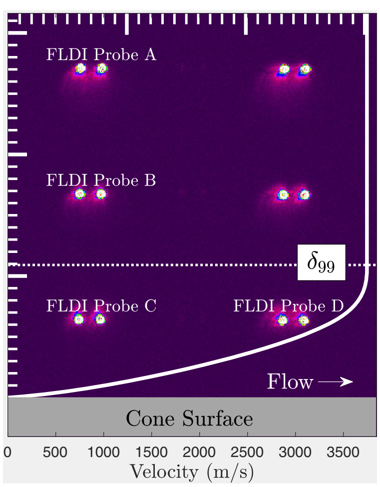

Fig. 4 Relative wall-normal and streamwise spacing of FLDI beam pairs for shot 2990.

adjustable iris diaphragm used to limit the amount of light to avoid image saturation. The beam was expanded using a plano-convex lens, collimated by a parabolic mirror, and directed through the test section using multiple planar mirrors. Downbeam of the test section, another parabolic mirror focused the beam to a point where a knife edge was inserted. The beam next passed through a bandpass filter to minimize test-gas luminosity from obscuring the image, and a series of plano-convex lenses were used to increase the image magnification. The images were recorded using a high-speed camera at a frame rate of 666 kHz with a resolution of 1280×64 pixels, providing a spatial scale of 0.13 mm/pixel. The field of view was approximately 17 cm in the streamwise direction and 7 cm in the wall-normal direction, starting approximately 59 cm from the nose tip.

III. Numerical Methods

Steady, basic-state flow solutions were calculated using a variety of well-established compressible CFD codes. The flow conditions were representative of the California Institute of Technology's T5 free-piston reflected shock tunnel conditions given above. The traditional approach to hypersonic stability analysis was utilized. First, the geometry of interest was generated, and a computational mesh was created with special attention paid to the boundary-layer resolution. The steady-state solutions (basic states) were calculated using the software of choice, and the flowfield was visualized. Finally, a stability analysis of the generated basic states was conducted with the selected stability solver.

A. Basic State Solvers

1. US3D

In US3D, the base flow over the cone was calculated using the tunnel freestream conditions identified in Table 2 and the wall-temperature distribution shown in Fig. 2. The typical mesh dimensions for the hypersonic stability analysis of a cone were roughly 1600 streamwise points with one degree rotation in the azimuthal direction, representing one cell width, and test-driven convergence to determine the number of wall normal points. The other boundary conditions were defined as an outflow at the downstream end of the domain and symmetry conditions on both azimuthal sides. Additional settings included high-temperature effects for a multispecies gas (five-species air: N_2, O_2, NO, N, O) in thermochemical nonequilibrium and laminar, viscous flow. Using CFL ramping, the calculation was run until it converged, and a steady-state solution was reached. Sutherland viscosity with K based on the first species model was utilized to analyze species viscosity, and diffusion coefficients were derived from the constant Lewis number. Thermal conductivity was related through the Eucken relation and viscosity. NASA Lewis data was utilized to model vibration-electronic energy relaxation. Additional details regarding implementation can be found in Candler [48].

2. DPLR

The STABL software package [15,45] uses a two-dimensional/axisymmetric mean flow solver based on NASA's implicit data-parallel line relaxation (DPLR) method [49]. The STABL DPLR solver uses an extended set of the Navier–Stokes equations incorporating high-temperature effects with a two-temperature model to characterize the translational, rotational, and vibrational modes and assuming five-species air (N_2, O_2, NO, N, O), with the gas mixture in thermal and chemical nonequilibrium. Additional details, including the governing equations used by the mean flow solver, can be found in Johnson [45] and Johnson and Candler [50].

The computational grid for the DPLR mean flow analysis was generated within the STABL software package. The grid was clustered near the tip of the cone and toward the cone's surface, with a minimum surface normal spacing chosen to maintain a y^+_{wall} value of less than one along the length of the cone. The grid-tailoring routine within STABL was employed to generate a refined, shock-fitted grid for the blunted cone models. The mean-flow analysis was rerun using the tailored grid to produce a high-quality mean-flow solution to input into the stability analysis.

3. CHAMPS

The curvilinear thermochemical nonequilibrium multispecies framework of CHAMPS was also utilized to obtain baseflows for each experiment. The multispecies gas (five-species air: N_2, O_2, NO, N, O) flow over the blunt cone was solved using a fifth-order accurate WENO flux reconstruction (Rusanov flux function), second-order accurate viscous discretization, and DPLR implicit time integration scheme. The Blottner model was used to evaluate the species viscosities, Eucken's relations to compute the species thermal conductivities for the translational/rotational and vibrational energy modes, and Wilke's mixing rule for mixture transport properties [51]. Additional details regarding the thermochemical nonequilibrium implementation in CHAMPS can be found in the work of McQuaid and Brehm [52].

Boundary-layer profiles generated by each of the mean flow solvers used in this work at the experimental measurement location are presented in Fig. 5. Excellent agreement between the three solvers was observed in the velocity and density profiles for both shot 2990 and shot 3019. We note a slight difference in the temperature profile computed by US3D compared to the results from DPLR and CHAMPS curvilinear framework.

B. Stability Tools

1. MAMOUT

ONERA's local linear stability code, MAMOUT, is designed to compute the eigenmodes of boundary-layer profiles, assuming a slow variation of the base flow in both streamwise and crosswise directions and a fast variation along the wall normal coordinate. The Navier–Stokes equations are linearized around a given laminar base flow. The generalized eigenvalue problem is then discretized using a high-order, quasi-spectral, compact finite-difference scheme. Incompressible fluids or perfect gas flows can be addressed, as well as a reacting mixture in chemical equilibrium, described by a Mollier chart. For a prescribed frequency, the program provides the local wave number and growth rate of the unstable wave and the associated eigenfunctions. A given mode can be tracked automatically on a prescribed frequency range for a series of boundary-layer profiles, and the amplification coefficient (N-factor) is then integrated.

2. STABL

The stability analysis of the flow was performed using PSE-Chem, the parabolized stability equation (PSE) solver within STABL. PSE-Chem was also used to solve the linear stability theory (LST) equations, which it does by making the "locally parallel" assumption that the mean flow only varies in the body-normal direction. The LST analysis begins by first estimating the disturbance frequency range, which is estimated by PSE-Chem using the characteristic time of wave travel between the wall and the relative sonic line [50]. Wavenumber guesses are evaluated using LST, and the most unstable converged solution at each frequency is retained. These results are used as initial values for the PSE analysis. PSE-Chem solves the linear parabolized stability equations derived from the axisymmetric Navier–Stokes equations [50]. The second-order partial differential equations generated from perturbing the mean flow with a fluctuating component and substituting into the Navier–Stokes equations are parabolized, and an initial solution is generated by assuming small initial disturbances and "locally parallel" flow at the starting plane [53]. The initial solution is marched downstream by simultaneously updating the complex streamwise wavenumber and the disturbance shape function [50]. Boundary-layer transition is predicted by PSE-Chem using the semi-empirical e^N correlation method [50], where N is the N-factor.

For the experiments analyzed, the stability analysis was performed using a single, highly concentrated stability grid with frequencies ranging from 850 to 3000 kHz and spanning the extent of the 99-cm-long cone.

3. JoKHeR

The JoHKeR Parabolized Stability Equations (PSE) package [54–56] was developed in collaboration with Dr. Helen Reed at Texas A&M as part of the efforts of the National Center for Hypersonic Laminar-Turbulent Transition Research. The code employs a quasi-3D, compressible, ideal gas, primitive variable formulation; that is, it marches disturbances along a predefined path with the assumption of uniformity in the perpendicular direction. The package consists of linear stability theory (LST), linear parabolized stability equation (LPSE), and nonlinear parabolized stability equation (NPSE) codes. These codes have been extensively validated against experimental [57–59] and numerical [60–62] datasets. A unique feature of JoHKeR is that it employs a nonlinear wave packet formulation for NPSE implementation that allows for the modeling of finite bandwidth disturbances [55,63] and thus accounts for spectral broadening and low-frequency content generation [64], which is important for accurate prediction of nonlinear energy exchange [65].

a. Linear Stability Theory. LST considers a steady basic flow state, determined from separate CFD simulations, and solves the disturbance

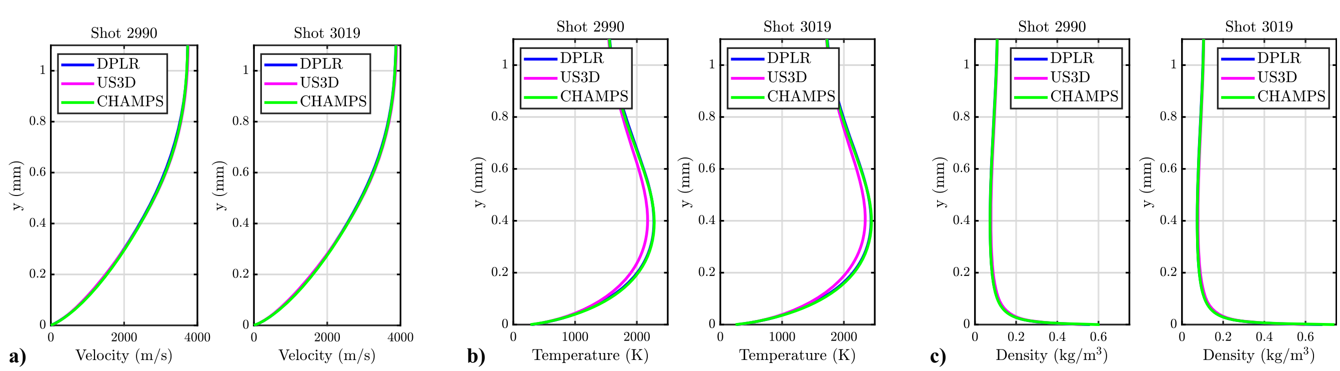

Fig. 5 a) Velocity, b) temperature, and c) density boundary-layer profiles for shots 2990 and 3019.

equation (which follows from substitution of Eq. (1) into the Navier–Stokes equations) assuming linear, parallel flow. The disturbance is assumed to be of the form indicated by Eq. (2), substitution of which into the disturbance equations leads to the generalized eigenvalue problem, with α and ω being the streamwise wave number and the frequency, respectively. The resulting eigenvalues are used to determine instability, and the corresponding eigenvectors represent the shape of the disturbance in the wall-normal direction.

$$\phi(x,y,z,t) = \underbrace{\bar{\phi}(y)}_{\text{basic state}} + \underbrace{\phi'(x,y,z,t)}_{\text{disturbance}} \tag{1}$$

$$\phi' = \hat{\phi}(y)e^{i(\alpha x+\beta z-\omega t)} \tag{2}$$

b. Parabolized Stability Equations. Originally identified by Herbert and Bertolotti [66] during a critical review of Gaster's [67] early nonparallel work, the parabolized stability equations have been developed as an efficient and powerful tool for studying the stability of advection-dominated laminar flows. Excellent introductions to the PSE method and a summary of its early development are provided by Herbert [68]. During the early stages of both linear and nonlinear development of this technique, much was established related to basic marching procedures, curvature, normalization conditions, and numerical stability of the method itself [69,70]. In a relatively short time, the field rapidly expanded to include complex geometries, compressible flow, and finite-rate thermodynamics.

PSE is similar to the Fourier/Laplace transform in that it considers an initial-value problem. However, the slowly varying basic state assumption is made in the streamwise direction, and a slow variable $\bar{x} = (x/Re)$ is introduced. Ultimately, disturbances are assumed to be of the form

$$F[\phi'] = \underbrace{\tilde{\phi}(\bar{x},y)}_{\text{shape}}\,\underbrace{\Phi(x,t)}_{\text{wave}}$$

where the wave part satisfies

$$\frac{\partial\Phi}{\partial x} = i\alpha(\bar{x})\Phi \tag{3}$$

$$\frac{\partial\Phi}{\partial t} = -i\omega\Phi \tag{4}$$

where $Re = (U_e\delta_r/\nu_e)$ is a Reynolds number based on the characteristic values of edge velocity (U_e), edge kinematic viscosity (ν_e), and reference boundary-layer length scale (δ_r). Thus, PSE considers disturbances of the form

$$\phi' = \int_{-\infty}^{\infty} \underbrace{\tilde{\phi}(\bar{x},y,\omega)}_{\text{shape}}\,\underbrace{A(\bar{x},\omega)e^{-i\omega t}}_{\text{wave}}\,\mathrm{d}\omega \tag{5}$$

where $A(\bar{x},\omega) = e^{i\int\alpha(\bar{x},\omega)\mathrm{d}x}$ and the dependence of the shape function ($\tilde{\phi}$) and amplitude function (A) on ω has been made explicit. The shape and amplitude functions are essentially the Fourier transform of the disturbance. Upon expansion of the streamwise derivatives

$$\frac{\partial\phi'}{\partial x} = \int_{-\infty}^{\infty}\left(\frac{1}{Re}\frac{\partial\tilde{\phi}}{\partial\bar{x}} + i\alpha\tilde{\phi}\right)Ae^{-i\omega t}\mathrm{d}\omega$$
$$\frac{\partial^2\phi'}{\partial x^2} = \int_{-\infty}^{\infty}\left(\frac{1}{Re^2}\frac{\partial^2\tilde{\phi}}{\partial\bar{x}^2} + \frac{2i\alpha}{Re}\frac{\partial\tilde{\phi}}{\partial\bar{x}} + \frac{i\tilde{\phi}}{Re}\frac{\partial\alpha}{\partial\bar{x}} - \alpha^2\tilde{\phi}\right)Ae^{-i\omega t}\mathrm{d}\omega$$

it is found that the second spatial derivative $\partial^2\tilde{\phi}/\partial\bar{x}^2$ is of the highest order, and a perturbation expansion may be consistently truncated, resulting in the neglect of this term. This leaves the disturbance equation nearly parabolized [70], and an efficient marching solution may be sought. JoKHeR implements a wave packet formulation [55,63], which appears to better represent energy transfer between modes in a nonlinear calculation. Ultimately, in the quasi-3D formulation, the disturbance is discretely represented as $\phi' = \sum_k\tilde{\phi}(\bar{x},y)_kA(\bar{x})_kW(\omega)_ke^{-i\omega_kt}$, and frequency content for each mode is assumed of the form $W_0 = (1/\sigma_0\sqrt{2\pi})e^{-((\omega-\omega_0)^2/2\sigma_0^2)}$. With bandwidth of the harmonics obeying $\sigma_i = \sqrt{i+1}\sigma_0$, and harmonic balancing is used to calculate nonlinear interactions. This representation of spectral energy appears to be crucial for modeling the spectral broadening seen in experiments. Note that all perturbation quantities presented in this manuscript are nondimensionalized in the standard way. Their amplitudes are normalized such that the temperature perturbation's maximum amplitude is unity.

4. CHAMPS

The University of Maryland's disturbance flow formulation solves either the nonlinear disturbance equations (NLDEs) or linear disturbance equations (LDEs) using either an overset mesh approach (AMR-WPT, see Refs. [71] and [72]) or curvilinear mesh approach. In this work, the LDEs were solved on curvilinear grids that conform to the surface of the cone. The base flow states for each experimental shot were also obtained with the curvilinear framework of CHAMPS; however, those obtained with US3D were utilized as well for easier comparison.

After eliminating the pure base flow contribution to the governing compressible Navier–Stokes equations, assuming that the base flow has been adequately converged to a steady-state solution (see Ref. [73] for more details), the final form of the nonlinear disturbance equations can be cast in the form

$$\frac{\partial\tilde{\boldsymbol{W}}}{\partial t} + \frac{\partial\tilde{\boldsymbol{E}}}{\partial x} + \frac{\partial\tilde{\boldsymbol{F}}}{\partial y} + \frac{\partial\tilde{\boldsymbol{G}}}{\partial z} = 0 \tag{6}$$

where the total flux vectors $\tilde{\boldsymbol{E}}$, $\tilde{\boldsymbol{F}}$, and $\tilde{\boldsymbol{G}}$ are a function of $\bar{\boldsymbol{W}}$ and $\tilde{\boldsymbol{W}}$ and its gradients. At the moment, the main ability for incorporating high-enthalpy gas effects in the simulations performed with CHAMPS is through interpolation of the transport properties of the precomputed basic state onto the disturbance mesh. Finally, the time derivative in Eq. (6) is replaced by a spectral differentiation operator, which transforms the problem to the frequency domain. Thus, the only assumption placed upon the disturbance field is that it is harmonic in time, viz.,

$$\phi' = \hat{\phi}(x,y,z)e^{-i\omega t} \tag{7}$$

The convective and viscous flux derivatives are discretized using a fifth-order WENO scheme and second-order centered viscous scheme as detailed in Browne et al. [73]. The resulting discrete system of equations is inverted for a given frequency using MUMPS through the PETSc framework [74]. More details of this "time-spectral/harmonic linearized Navier–Stokes equations" (TS/HLNSE) approach can be found in Haas et al. [75]. All CHAMPS disturbance flow calculations will henceforth be referred to as "TS," which is a linear calculation.

A summary of the different computational methods used in this work is presented in Table 3.

IV. Results

A. Experimental

We begin by presenting experimental results for the previously discussed experiments performed at T5. Shot 2990 represented an experiment during which the cone's surface was not actively cooled, with a transitional boundary layer at relatively high enthalpy (8.9 MJ/kg). The averaged power spectral density (PSD) for this experiment, computed from measurements taken by the FLDI diagnostic, is shown in Fig. 6a. The upstream and downstream probes within the boundary layer show distinct peaks representing the second-mode instability at approximately $f_{2M} \approx 1250$ kHz. Elevated low-frequency spectral content is observed by the probes

Table 3 Summary of stability solvers

	Base state			Stability analysis	
Solver	Source	Boundary conditions	Assumptions	Dist. Eq.	Boundary conditions
STABL	DPLR	Wall: no-slip, isothermal (prescribed by exp. measurements), zero mass concentration gradient and pressure gradient normal to the surface Outflow: supersonic	TCNE w/5 sp. air Two-temp. model Reaction rates: Park 1990 [76] Transport method: BEW	LPSE with TCNE effects	Wall: velocity, temperature disturbances, and pressure gradients equal zero Outer boundary: zero disturbances in all variables
MAMOUT	US3D	Wall: no-slip for velocity, isothermal (prescribed by experimental measurements)	TCNE w/5 sp. air Reaction rates: Park 1990 [76]	LST with CEQ effects	Thermochemical equilibrium with quantities interpolated in a Mollier diagram Wall: zero velocity and temperature fluctuations Outer boundary: matching condition
JoKHeR	US3D	Wall: no-slip for velocity, isothermal (prescribed by experimental measurements)	TCNE w/5 sp. air Reaction rates: Park 1990 [76]	LPSE with PG effects	Wall: no-slip velocity, zero temperature perturbation, $dT'/dz = 0$ for adiabatic simulations, mass equation for density Outer boundary: zero disturbances in all variables
CHAMPS	US3D	Wall: no-slip for velocity, isothermal (prescribed by experimental measurements)	TCNE w/5 sp. air Reaction rates: Park 1990 [76] Perfect gas	TS/HLNSE with baseflow transport properties	Inflow and top: Dirichlet Wall: no-slip velocity, Dirichlet for temperature, Neumann for pressure Outflow: extrapolate all variables
	CHAMPS	Wall: no-slip, isothermal (prescribed by exp. measurements), zero mass concentration gradient and pressure gradient normal to the surface Outflow: supersonic	TCNE w/5 sp. air Two-temp. model Reaction rates: Park 1989 [77] Transport method: BEW		

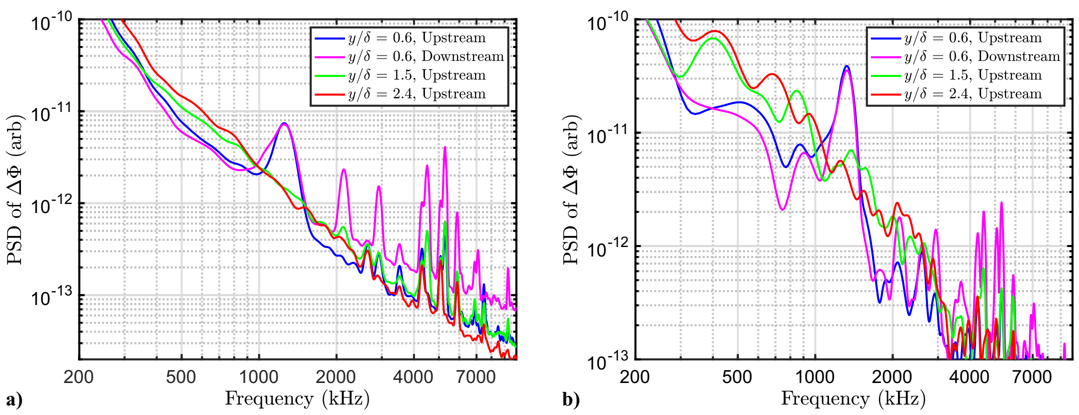

Fig. 6 a) Averaged and b) short-time PSD for shot 2990.

outside of the boundary layer. The distinct peaks at approximately 2100 and 2900 kHz seen in the downstream FLDI probe at $y/\delta = 0.6$ were found to exist before flow onset and determined to originate from the baseline noise signal. To further investigate a second-mode disturbance observed during the test time, we perform a short-time Fourier transform centered in time around the emergence of the second-mode instability. The resulting short-time PSD is presented in Fig. 6b. Here, in addition to the second-mode instability being measured by the FLDI probes positioned inside the boundary layer, the first harmonic of the instability is also observed at approximately 2600 kHz. Higher-order spectral analysis was used to verify the presence of quadratic phase-coupled interactions generating this harmonic through nonlinear processes [38,78].

Shot 3019 featured an actively cooled cone. High-speed schlieren was used to investigate boundary-layer instabilities for this experiment. Spatial pixel intensities from schlieren frames were converted to reconstructed time signals for each location within the boundary layer. The reconstructed time signal at approximately $y/\delta = 0.25$ was assessed using a discrete Fourier transform. The resulting averaged PSD is shown in Fig. 7. The spectra show a peak second-mode frequency of approximately 1235 kHz, with a slightly lower peak at approximately 1200 kHz.

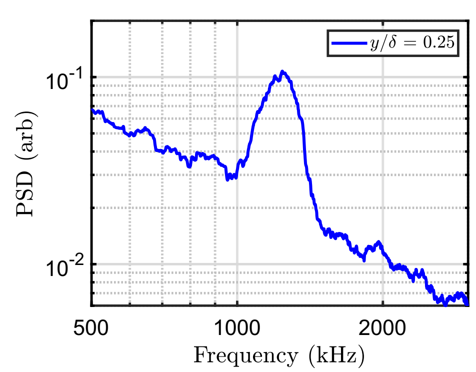

Fig. 7 Averaged PSD for shot 3019.

B. Numerical

Stability calculations from ONERA's MAMOUT (LST solver assuming gas mixture under chemical equilibrium), University of Delaware's JoKHeR (LPSE solver assuming perfect gas effects), Stevens Institute of Technology's version of STABL (LPSE solver

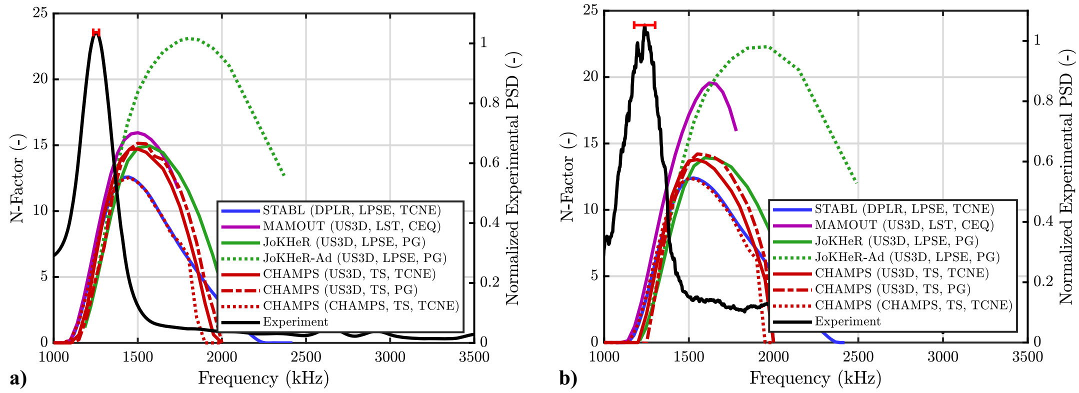

Fig. 8 Comparison between experimental and numerical results for shots a) 2990 and b) 3019.

assuming gas mixture under thermochemical nonequilibrium), and University of Maryland's CHAMPS (TS/HLNSE solver considering baseflow transport properties) are compared amongst each other and with experimental results in Fig. 8. Each numerical group was given the run conditions and geometry of interest and asked to calculate the boundary-layer instabilities. The goal of this comparison was to begin understanding the range of predictability using different stability approaches for high-enthalpy flows. N-factors were extracted from each numerical calculation at the point corresponding to the experimental data collection site. For reference, the source of the base flow (DPLR, US3D, and CHAMPS curvilinear framework), disturbance equations solved (LST, LPSE, and TS), and the gas behavior assumed by the disturbance equations (TCNE: gas mixture in thermochemical nonequilibrium; CEQ: gas mixture in chemical equilibrium; PG: perfect gas) are provided in the legend. The experimental results are also presented in this figure. For shot 2990, the spectra generated from data collected by the upstream FLDI probe within the boundary layer is shown. Although not the appropriate boundary condition in the experiment, for academic purposes, we performed simulations with the JoKHeR stability solver assuming an adiabatic boundary condition. We also include these N-factor results for further discussion.

Several trends are observed for the shots considered:

1) For both the uncooled (shot 2990, FLDI diagnostic) and cooled (shot 3019, schlieren diagnostic) experiments, all stability solvers predicted a higher most amplified frequency than the experimentally measured second-mode frequency. It is fairly well-established that the second-mode frequency is closely tied to the boundary-layer length scale in the sense of the thermoacoustic resonance mechanism. However, for high-enthalpy flows, the boundary-layer height is affected by finite-rate chemistry dynamics. Therefore, the most accurate numerical prediction of the most amplified frequency was expectedly achieved by the solvers that considered gas mixtures in thermal and chemical nonequilibrium. Nevertheless, the stability solvers were generally inaccurate in predicting the most amplified frequency when compared to the experimentally measured second-mode frequency, with an estimated error of 16–24% for shot 2990 and 23–33% for shot 3019. This discrepancy could be due to errors in the computed run condition. That is, variations in the freestream temperature and species partial pressure during the test time, as measured by Girard et al. [79] for similar conditions at T5, may not be adequately considered in the run condition calculation. Further investigation is necessary to better understand the effect of this difference on stability analysis.

2) For the two experiments analyzed, excellent agreement in terms of peak N-factor and most amplified frequency was observed between STABL and the CHAMPS stability analysis performed using the CHAMPS curvilinear framework baseflow. These solvers showed a peak N-factor of approximately $N = 12.6$ at 1450 kHz for shot 2990 and $N = 12.4$ at 1550 kHz for shot 3019. Regarding these two metrics, good agreement was observed among the stability solvers utilizing the US3D baseflow with a peak N-factor of approximately $N = 15$ at 1500 kHz for shot 2990 and approximately $N = 14$ at 1600 kHz for shot 3019. A notable exception to the consistency of these results was observed in the MAMOUT stability computation for shot 3019, which exhibited a significant sensitivity to wall cooling, with the N-factor increasing to $N = 19$. Furthermore, for both experiments, the simulations performed using the CHAMPS stability solver showed the disturbance remained amplified until approximately 2000 kHz, whereas the JoKHeR results suggested the disturbance amplification region extended to frequencies greater than 2000 kHz.

3) There was a moderate amount of uncertainty in the predicted most amplified frequency and a significant amount of uncertainty in the predicted peak N-factor magnitude observed among the stability solvers. This spread was somewhat surprising when compared to similar studies conducted in low-enthalpy quiet tunnels [59]. In regard to the precision of the most amplified frequency prediction, the various stability solvers were generally in good agreement. The solvers computed a frequency range of approximately 1450–1550 kHz for shot 2990 and approximately 1525–1650 kHz for shot 3019. Although the results from MAMOUT predicted exceptionally high disturbance amplification with wall cooling, the most amplified frequency predicted by this solver experienced only a modest increase within the previously identified range. We observed significant imprecision among the various stability solvers in terms of N-factor magnitude prediction. The peak N-factor ranged from $N = 12.5$–16 for shot 2990 and from $N = 12.3$–19 for shot 3019. The JoKHeR simulations performed using the adiabatic boundary condition fell outside of the previously identified ranges for most amplified frequency and N-factor, predicting $N = 23$ at 1800 kHz for shot 2990 and $N = 22$ at 1970 kHz for shot 3019.

4) Considering the N-factor magnitude predicted by the CHAMPS stability simulations, we observed a high degree of sensitivity to the baseflow. For shot 2990, the CHAMPS simulations performed using the US3D baseflow showed a peak N-factor of approximately 15, while the simulation performed using the CHAMPS curvilinear baseflow showed a peak N-factor of approximately 12. Although not as drastic, a corresponding decrease was also observed for shot 3019. While the CHAMPS stability results seem to be sensitive to the selected baseflow, they align with results from other stability solvers using a similar or equivalent baseflow. That is, when the US3D baseflow was used for the CHAMPS stability simulation, the stability results aligned with those obtained from other stability solvers using the US3D baseflow (JoKHeR and MAMOUT), and when the CHAMPS stability simulation used the CHAMPS curvilinear framework baseflow, which matched the DPLR baseflow, the results matched the DPLR-based stability results obtained using STABL. Regardless, this level of sensitivity was unexpected given the similarity of the baseflow profiles presented in Fig. 5. Further investigation is necessary to determine if it extends to other stability solvers.

5) Comparing the computational results of shot 2990 to shot 3019, we observed an increase of approximately 100 kHz in the most amplified frequency. As an average of the stability results, the most amplified frequency increased from approximately 1500 kHz

for shot 2990 to approximately 1600 kHz for shot 3019. Additionally, there is a general decrease in peak N-factor with wall cooling. The decrease in peak N-factor was most prevalent amongst stability solvers that utilized the US3D baseflow. Contrasting these results, we observed significant destabilization due to wall cooling predicted by MAMOUT, the LST-based solver.

6) The JoKHeR LPSE code was run with isothermal and, as an academic investigation, adiabatic boundary conditions for the temperature disturbance. The most amplified frequency and peak N-factor predicted by JoKHeR demonstrated tremendous sensitivity to the Dirichlet or Neumann boundary conditions on disturbance temperature. It is theoretically expected the adiabatic wall boundary condition will change the particular resonant structure within the boundary layer. In this case, it appears to have strengthened the resonance. Further work is required to quantify this behavior; specifically, an energetics investigation may provide additional understanding.

V. Conclusions

Results gathered from experiments at Caltech's T5 free-piston reflected shock tunnel were compared with N-factor calculations performed using various numerical stability solvers. Two experiments (shot 2990 and shot 3019) were analyzed, both featuring a blunt cone and a highly cooled boundary layer. For shot 2990, the surface of the cone remained at room temperature, and the boundary layer was probed using FLDI. For shot 3019, active cooling using liquid nitrogen was able to achieve a moderate decrease in the cone's surface temperature, and experimental measurements of the second-mode disturbance were made using schlieren. For both experiments, each diagnostic technique measured a strong second-mode disturbance within the boundary layer.

Numerical stability simulations were computed using the provided experimental run conditions. For each experiment, the accuracy of each stability solver was evaluated with a comparison of the computed most amplified frequency to the experimentally measured second-mode frequency. The stability solvers that considered gas mixtures in thermochemical nonequilibrium best agreed with the measured second-mode frequency. However, they overpredicted the most amplified frequency by approximately 16% for shot 2990 and 23% for shot 3019. A moderate variation in the most amplified frequency predicted by each solver was also observed, ranging from 1450 to 1550 kHz for shot 2990 and 1525 to 1650 kHz for shot 3019.

The stability solvers used in this work were generally inconsistent in predicting the peak N-factor magnitude. Disregarding outliers, the computed N-factor profiles seemed to be categorized into two groups based on the utilized baseflow. Excellent agreement was achieved between STABL and the CHAMPS stability simulation performed using the CHAMPS curvilinear framework baseflow. For shot 2990, reasonable agreement was achieved among the various stability solvers that used the US3D baseflow (MAMOUT, JoKHeR, and CHAMPS performed with the US3D baseflow), which assumed either chemical equilibrium, thermochemical nonequilibrium, or perfect gas effects. This consensus deteriorated for shot 3019, as MAMOUT's LST-based solver predicted a dramatically destabilized disturbance. Across these two groupings, the computed peak N-factor magnitude ranged from 12.5 to 16 for shot 2990 and 12.3 to 19 for shot 3019. This wide range in the predicted peak N-factor is concerning and necessitates further investigation.

In summary, this comparison demonstrates the difficulty in predicting transition at high enthalpy. The comparison among the four stability solvers indicates a strong sensitivity to the base flow. Small differences between the base flow, as shown in the boundary-layer profiles in Fig. 5, appear to result in large disparities in the predicted N-factor. The consistent overprediction of the most amplified frequency (as compared to the measured second-mode frequency) by the four stability solvers suggests greater attention needs to be given to the run condition calculation and effects of nonlinearity and experimental conditions (e.g., small angles of attack) for high-enthalpy hypersonic boundary-layer stability analysis.

Acknowledgments

The authors would like to thank James Chen and Vincenzo Russo for their support in performing stability analyses included in this work. The authors would also like to thank Dr. Joanna Austin and Dr. Wesley Yu, and acknowledge the expertise of Noel Esparza-Duran in operating Caltech's T5 reflected shock tunnel. Ahsan Hameed, Nick Parziale, and Laura Paquin were supported for this work by Air Force Office of Scientific Research (AFOSR) grant FA9550-18-1-0403. Support for the Parziale group was also provided by Office of Naval Research (ONR) grants N00014-20-1-2549 and N00014-23-1-2474. Joseph Kuehl, Tony Liang, and Kevin Graziose were supported by AFOSR grant number FA9550-22-1-0017. Sean Dungan and Christoph Brehm would like to acknowledge the financial support provided by the National Science Foundation (NSF) under CBET-2146100, as well as AFOSR under FA9550-22-1-0464. Sean Dungan was also supported by the Department of Defense (DoD) through the National Defense Science & Engineering Graduate (NDSEG) Fellowship Program. The authors would like to thank the program officers at AFOSR (Ivett Leyva, Sarah Popkin, Amanda Chou), ONR (Eric Marineau), and NSF (Ronald Joslin) for their support of this collaboration.

References

[1] Schneider, S. P., "Flight Data for Boundary-Layer Transition at Hypersonic and Supersonic Speed," *Journal of Spacecraft and Rockets*, Vol. 36, No. 1, 1999, pp. 8–20.
https://doi.org/10.2514/2.3428

[2] MacLean, M., Wadhams, T., Holden, M., and Johnson, H., "Ground Test Studies of the HIFiRE-1 Transition Experiment Part 2: Computational Analysis," *Journal of Spacecraft and Rockets*, Vol. 45, No. 6, 2008, pp. 1149–1164.
https://doi.org/10.2514/1.37693

[3] DSB, "Report of the Defense Science Board Task Force on the National Aerospace Plane (NASP)," AD-A201 124, 1988.

[4] Sherman, M., and Nakamura, T., "Flight Test Measurements of Boundary-Layer Transition on a Nonablating 22 Deg Cone," *Journal of Spacecraft and Rockets*, Vol. 7, No. 2, 1970, pp. 137–142.
https://doi.org/10.2514/3.29888

[5] Malik, M. R., "Hypersonic Flight Transition Data Analysis Using Parabolized Stability Equations with Chemistry Effects," *Journal of Spacecraft and Rockets*, Vol. 40, No. 3, 2003, pp. 332–344.
https://doi.org/10.2514/2.3968

[6] Lees, L., "The Stability of the Laminar Boundary Layer in a Compressible Fluid," NASA TN, 1947.

[7] Mack, L. M., "Review of Linear Compressible Stability Theory," *Stability of Time Dependent and Spatially Varying Flows: Proceedings of the Symposium on the Stability of Time Dependent and Spatially Varying Flows*, Springer-Verlag, Berlin, 1987, pp. 164–187.
https://doi.org/10.1007/978-1-4612-4724-1_9

[8] Mack, L., "Effect of Cooling on Boundary-Layer Stability at Mach Number 3," *Instabilities and Turbulence in Engineering Flows*, Springer, Berlin, 1993, pp. 175–188.
https://doi.org/10.1007/978-94-011-1743-2_9

[9] Bitter, N. P., and Shepherd, J. E., "Stability of Highly Cooled Hypervelocity Boundary Layers," *Journal of Fluid Mechanics*, Vol. 778, No. 10, 2015, pp. 586–620.
https://doi.org/10.1017/jfm.2015.358

[10] Knisely, C. P., and Zhong, X., "Sound Radiation by Supersonic Unstable Modes in Hypersonic Blunt Cone Boundary Layers. I. Linear Stability Theory," *Physics of Fluids*, Vol. 31, No. 2, 2019, Paper 024103.
https://doi.org/10.1063/1.5055761

[11] Knisely, C. P., and Zhong, X., "Sound Radiation by Supersonic Unstable Modes in Hypersonic Blunt Cone Boundary Layers. II. Direct Numerical Simulation," *Physics of Fluids*, Vol. 31, No. 2, 2019, Paper 024104.
https://doi.org/10.1063/1.5077007

[12] Chuvakhov, P. V., and Fedorov, A. V., "Spontaneous Radiation of Sound by Instability of a Highly Cooled Hypersonic Boundary Layer," *Journal of Fluid Mechanics*, Vol. 805, Oct. 2016, pp. 188–206.
https://doi.org/10.1017/jfm.2016.560

[13] Unnikrishnan, S., and Gaitonde, D. V., "Instabilities and Transition in Cooled Wall Hypersonic Boundary Layers," *Journal of Fluid Mechanics*, Vol. 915, May 2021, Paper A26.
https://doi.org/10.1017/jfm.2021.84

[14] Chang, C. L., Vinh, H., and Malik, M. R., "Hypersonic Boundary-Layer Stability with Chemical Reactions Using PSE," *28th Fluid Dynamics Conference*, AIAA Paper 1997-2012, 1997.
https://doi.org/10.2514/6.1997-2012

[15] Johnson, H. B., Seipp, T. G., and Candler, G. V., "Numerical Study of Hypersonic Reacting Boundary Layer Transition on Cones," *Physics of Fluids*, Vol. 10, No. 13, 1998, pp. 2676–2685.
https://doi.org/10.1063/1.869781

[16] Adam, P. H., and Hornung, H. G., "Enthalpy Effects on Hypervelocity Boundary-Layer Transition: Ground Test and Flight Data," *Journal of Spacecraft and Rockets*, Vol. 34, No. 5, 1997, pp. 614–619.
https://doi.org/10.2514/2.3278

[17] Germain, P. D., and Hornung, H. G., "Transition on a Slender Cone in Hypervelocity Flow," *Experiments in Fluids*, Vol. 22, No. 3, 1997, pp. 183–190.
https://doi.org/10.1007/s003480050036

[18] Vidal, R., and Golian, T., "Heat-Transfer Measurements with a Catalytic Flat Plate in Dissociated Oxygen," *AIAA Journal*, Vol. 5, No. 9, 1967, pp. 1579–1588.
https://doi.org/10.2514/3.4254

[19] East, R., Stalker, R., and Baird, J., "Measurements of Heat Transfer to a Flat Plate in a Dissociated High-Enthalpy Laminar Air Flow," *Journal of Fluid Mechanics*, Vol. 97, No. 4, 1980, pp. 673–699.
https://doi.org/10.1017/S0022112080002753

[20] Germain, P., "The Boundary Layer on a Sharp Cone in High-Enthalpy Flow," Ph.D. Thesis, California Inst. of Technology, Pasadena, CA, 1993.

[21] Adam, P., "Enthalpy Effects on Hypervelocity Boundary Layers," Ph.D. Thesis, California Inst. of Technology, Pasadena, CA, 1997.

[22] Rasheed, A., "Passive Hypervelocity Boundary Layer Control Using an Acoustically Absorptive Surface," Ph.D. Thesis, California Inst. of Technology, Pasadena, CA, 2001.

[23] Rasheed, A., Hornung, H. G., Fedorov, A. V., and Malmuth, N. D., "Experiments on Passive Hypervelocity Boundary-Layer Control Using an Ultrasonically Absorptive Surface," *AIAA Journal*, Vol. 40, No. 3, 2002, pp. 481–489.
https://doi.org/10.2514/2.1671

[24] Fujii, K., and Hornung, H. G., "A Procedure to Estimate the Absorption Rate of Sound Propagating Through High Temperature Gas," GALCIT Rept. 2001.004, 2001.

[25] Leyva, I. A., Laurence, S. J., Beierholm, A. K., Hornung, H. G., Wagnild, R. M., and Candler, G. V., "Transition Delay in Hypervelocity Boundary Layers by Means of CO_2/Acoustic Instability Interactions," *Proceedings of 47th AIAA Aerospace Sciences Meeting Including the New Horizons Forum and Aerospace Exposition*, AIAA Paper 2009-1287, 2009.
https://doi.org/10.2514/6.2009-1287

[26] Leyva, I. A., Jewell, J. S., Laurence, S. J., Hornung, H. G., and Shepherd, J. E., "On the Impact of Injection Schemes on Transition in Hypersonic Boundary Layers," *Proceedings of 16th AIAA/DLR/DGLR International Space Planes and Hypersonic Systems and Technologies Conference*, AIAA Paper 2009-7204, 2009.
https://doi.org/10.2514/6.2009-7204

[27] Jewell, J. S., Leyva, I. A., Parziale, N. J., and Shepherd, J. E., "Effect of Gas Injection on Transition in Hypervelocity Boundary Layers," *Proceedings of the 28th International Symposium on Shock Waves, ISSW-2767*, Springer, Berlin, 2011, pp. 735–740.
https://doi.org/10.1007/978-3-642-25688-2_111

[28] Jewell, J. S., Parziale, N. J., Leyva, I. A., and Shepherd, J. E., "Turbulent Spot Observations Within a Hypervelocity Boundary Layer on a 5-Degree Half-Angle Cone," *Proceedings of 42nd AIAA Fluid Dynamics Conference and Exhibit*, AIAA Paper 2012-3062, 2012.
https://doi.org/10.2514/6.2012-3062

[29] Jewell, J. S., Wagnild, R. M., Leyva, I. A., Candler, G. V., and Shepherd, J. E., "Transition Within a Hypervelocity Boundary Layer on a 5-Degree Half-Angle Cone in Air/CO_2 Mixtures," *Proceedings of 51st AIAA Aerospace Sciences Meeting Including the New Horizons Forum and Aerospace Exposition*, AIAA Paper 2013-0523, 2013.
https://doi.org/10.2514/6.2013-523

[30] Parziale, N. J., Jewell, J. S., Shepherd, J. E., and Hornung, H. G., "Optical Detection of Transitional Phenomena on Slender Bodies in Hypervelocity Flow," *Proceedings of RTO Specialists Meeting AVT-200/RSM-030 on Hypersonic Laminar-Turbulent Transition*, NATO, San Diego, CA, 2012.

[31] Parziale, N. J., Shepherd, J. E., and Hornung, H. G., "Differential Interferometric Measurement of Instability at Two Points in a Hypervelocity Boundary Layer," *Proceedings of 51st AIAA Aerospace Sciences Meeting Including the New Horizons Forum and Aerospace Exposition*, AIAA Paper 2013-0521, 2013.
https://doi.org/10.2514/6.2013-521

[32] Parziale, N. J., Shepherd, J. E., and Hornung, H. G., "Differential Interferometric Measurement of Instability in a Hypervelocity Boundary Layer," *AIAA Journal*, Vol. 51, No. 3, 2013, pp. 750–754.
https://doi.org/10.2514/1.J052013

[33] Parziale, N. J., "Slender-Body Hypervelocity Boundary-Layer Instability," Ph.D. Thesis, California Inst. of Technology, , Pasadena, CA, 2013.

[34] Tanno, H., Komuro, T., Sato, K., Itoh, K., Takahashi, M., and Fujii, K., "Measurement of Hypersonic Boundary Layer Transition on Cone Models in the Free-Piston Shock Tunnel HIEST," *Proceedings of 47th AIAA Aerospace Sciences Meeting Including the New Horizons Forum and Aerospace Exposition*, AIAA Paper 2009-0781, 2009.
https://doi.org/10.2514/6.2009-781

[35] Tanno, H., Komuro, T., Sato, K., Itoh, K., Takahashi, M., and Fujii, K., "Measurement of Hypersonic High-Enthalpy Boundary Layer Transition on a 7°cone Model," *48th AIAA Aerospace Sciences Meeting Including the New Horizons Forum and Aerospace Exposition*, AIAA Paper 2010-0310, 2010.
https://doi.org/10.2514/6.2010-310

[36] Laurence, S. J., Wagner, A., and Hannemann, K., "Experimental Study of Second-Mode Instability Growth and Breakdown in a Hypersonic Boundary Layer Using High-Speed Schlieren Visualization," *Journal of Fluid Mechanics*, Vol. 797, June 2016, pp. 471–503.
https://doi.org/10.1017/jfm.2016.280

[37] Hameed, A., Shekhtman, D., Parziale, N. J., Paquin, L. A., Skinner, S., Laurence, S. J., Yu, W. M., and Austin, J. M., "Hypersonic Boundary-Layer Instability on a Highly Cooled Cone. Part I: Q-FLDI Measurement and Instability Calculations," *Proceedings of AIAA Scitech 2022 Forum*, AIAA Paper 2022-0734, 2022.
https://doi.org/10.2514/6.2022-0734

[38] Hameed, A., Parziale, N. J., Paquin, L. A., Laurence, S. J., Yu, W. M., and Austin, J. M., "Characterization of Transitional, High-Enthalpy Boundary Layers on a Blunted Cone. Part II: FLDI and Higher Order Spectral Analysis," *Proceedings of AIAA Scitech 2023 Forum*, AIAA Paper 2023-0288, 2023.
https://doi.org/10.2514/6.2023-0288

[39] Paquin, L. A., Laurence, S. J., Hameed, A., Parziale, N. J., Yu, W. M., and Austin, J. M., "Characterization of Transitional, High-Enthalpy Boundary Layers on a Slightly-Blunted Cone. Part I: Schlieren Imaging," *Proceedings of AIAA Scitech 2023 Forum*, AIAA Paper 2023-0289, 2023.
https://doi.org/10.2514/6.2023-0289

[40] Hornung, H. G., "Performance Data of the New Free-Piston Shock Tunnel at GALCIT," *Proceedings of 28th Joint Propulsion Conference and Exhibit*, AIAA Paper 1992-3943, 1992.
https://doi.org/10.2514/6.1992-3943

[41] Goodwin, D. G., "An Open-Source, Extensible Software Suite for CVD Process Simulation," *Proceedings of CVD XVI and EuroCVD Fourteen*, edited by llendorf, M. , Maury, F., and Teyssandier, F., Electrochemical Society, Pennington, NJ, 2003, pp. 155–162.

[42] Browne, S., Ziegler, J., and Shepherd, J. E., "Numerical Solution Methods for Shock and Detonation Jump Conditions," GALCIT Rept. FM2006-006, Graduate Aerospace Lab., California Inst. of Technology, Pasadena, CA, 2006.

[43] Wright, M. J., Candler, G. V., and Prampolini, M., "Data-Parallel Lower-Upper Relaxation Method for the Navier-Stokes Equations," *AIAA Journal*, Vol. 34, No. 7, 1996, pp. 1371–1377.
https://doi.org/10.2514/3.13242

[44] Candler, G. V., "Hypersonic Nozzle Analysis Using an Excluded Volume Equation of State," *Proceedings of 38th AIAA Thermophysics Conference*, AIAA Paper 2005-5202, 2005.
https://doi.org/10.2514/6.2005-5202

[45] Johnson, H. B., "Thermochemical Interactions in Hypersonic Boundary Layer Stability," Ph.D. Thesis, Univ. of Minnesota, Minneapolis, MI, 2000.

[46] Wagnild, R. M., "High Enthalpy Effects on Two Boundary Layer Disturbances in Supersonic and Hypersonic Flow," Ph.D. Thesis, Univ. of Minnesota, Minnesota, MI, 2012.

[47] Paquin, L. A., Skinner, S., Laurence, S. J., Hameed, A., Shekhtman, D., Parziale, N. J., Yu, W. M., and Austin, J. M., "Hypersonic Boundary-Layer Instability on a Highly Cooled Cone. Part II: Schlieren Analysis of Boundary-Layer Disturbances," *Proceedings of AIAA Scitech*, AIAA Paper 2022-0947, 2022.
https://doi.org/10.2514/6.2022-0947

[48] Candler, G. V., Johnson, H. B., Nompelis, I., Subbareddy, P. K., Drayna, T. W., Gidzak, V., and Barnhardt, M. D., "Development of the US3D Code for Advanced Compressible and Reacting Flow

Simulations," *53rd AIAA Aerospace Sciences Meeting*, AIAA Paper 2015-1893, 2015.
https://doi.org/10.2514/6.2015-1893

[49] Wright, M. J., Candler, G. V., and Bose, D., "Data-Parallel Line Relaxation Method for the Navier-Stokes Equations," *AIAA Journal*, Vol. 36, No. 9, 1998, pp. 1603–1609.
https://doi.org/10.2514/2.586

[50] Johnson, H. B., and Candler, G. V., "Hypersonic Boundary Layer Stability Analysis Using PSE-Chem," *35th AIAA Fluid Dynamics Conference and Exhibit*, AIAA Paper 2005-5023, 2005.
https://doi.org/10.2514/6.2005-5023

[51] Zhang, H., "High Temperature Flow Solver for Aerothermodynamics Problems," Ph.D. Thesis, Univ. of Kentucky, Lexington, KY, July 2015.

[52] McQuaid, J. A., and Brehm, C., "Heat Flux Predictions for Hypersonic Flows with an Overset Near Body Solver on an Adaptive Block-Structured Cartesian Off-Body Grid," *Computers and Fluids*, Vol. 269, Jan. 2024, Paper 106121.
https://doi.org/10.1016/j.compfluid.2023.106121

[53] MacLean, M., Mundy, E., Wadhams, T., Holden, M., Johnson, H. B., and Candler, G. V., "Comparisons of Transition Prediction Using PSE-Chem to Measurements for a Shock Tunnel Environment," *37th AIAA Fluid Dynamics Conference and Exhibit*, AIAA Paper 2007-4490, 2007.
https://doi.org/10.2514/6.2007-4490

[54] Kuehl, J. J., Perez, E., and Reed, H. L., "JoKHeR: NPSE Simulations of Hypersonic Crossflow Instability," *50th AIAA Aerospace Sciences Meeting including the New Horizons Forum and Aerospace Exposition*, AIAA Paper 2012-0921, 2012.
https://doi.org/10.2514/6.2012-921

[55] Kuehl, J. J., "Discrete-and Finite-Bandwidth-Frequency Distributions in Nonlinear Stability Applications," *Physics of Fluids*, Vol. 29, No. 2, 2017.
https://doi.org/10.1063/1.4975158

[56] Perez, E., Reed, H. L., and Kuehl, J. J., "Instabilities on a Hypersonic Yawed Straight Cone," *43rd AIAA Fluid Dynamics Conference*, AIAA Paper 2013-2879, 2013.
https://doi.org/10.2514/6.2013-2879

[57] Hofferth, J. W., Saric, W. S., Kuehl, J., Perez, E., and Reed, H., "Boundary-Layer Instability and Transition on a Flared Cone in a Mach 6 quiet Wind Tunnel," *International Journal of Engineering Systems Modelling and Simulation*, Vol. 5, Nos. 1–3, 2013, pp. 109–124.
https://doi.org/10.1504/IJESMS.2013.052386

[58] Kocian, T. S., Perez, E., Oliviero, N. B., Kuehl, J. J., and Reed, H. L., "Hypersonic Stability Analysis of a Flared Cone," *Proceedings of 51st AIAA Aerospace Sciences Meeting Including the New Horizons Forum and Aerospace Exposition*, AIAA Paper 2013-0667, 2013.
https://doi.org/10.2514/6.2013-667

[59] Chynoweth, B. C., Schneider, S. P., Hader, C., Fasel, H., Batista, A., Kuehl, J., Juliano, T. J., and Wheaton, B. M., "History and Progress of Boundary-Layer Transition on a Mach-6 Flared Cone," *Journal of Spacecraft and Rockets*, Vol. 56, No. 2, 2019, pp. 333–346.
https://doi.org/10.2514/1.A34285

[60] Reed, H. L., Perez, E., Kuehl, J., Kocian, T., and Oliviero, N., "Verification and Validation Issues in Hypersonic Stability and Transition Prediction," *Journal of Spacecraft and Rockets*, Vol. 52, No. 1, 2015, pp. 29–37.
https://doi.org/10.2514/1.A32825

[61] Kuehl, J. J., and Paredes, P., "Gortler Modified Mack-Modes on a Hypersonic Flared Cone," *54th AIAA Aerospace Sciences Meeting*, AIAA Paper 2016-0849, 2016.
https://doi.org/10.2514/6.2016-0849

[62] Perez, E., Kocian, T. S., Kuehl, J. J., and Reed, H. L., "Stability of Hypersonic Compression Cones," *42nd AIAA Fluid Dynamics Conference and Exhibit*, AIAA Paper 2012-2962, 2012.
https://doi.org/10.2514/6.2012-2962

[63] Kuehl, J. J., Reed, H. L., Kocian, T. S., and Oliviero, N. B., "Bandwidth Effects on Mack-Mode Instability," *7th AIAA Theoretical Fluid Mechanics Conference*, AIAA Paper 2014-2777, 2014.
https://doi.org/10.2514/6.2014-2777

[64] Batista, A., and Kuehl, J. J., "A Mechanism for Spectral Broadening and Implications for Saturation Amplitude Estimates," *47th AIAA Fluid Dynamics Conference*, AIAA Paper 2017-3635, 2017.
https://doi.org/10.2514/6.2017-3635

[65] Kuehl, J. J., "Nonlinear Saturation Versus Nonlinear Detuning: Quantification on a Mach 6 Flared Cone," *55th AIAA Aerospace Sciences Meeting*, AIAA Paper 2017-0763, 2017.
https://doi.org/10.2514/6.2017-0763

[66] Herbert, T., and Bertolotti, F., "Stability Analysis of Nonparallel Boundary Layers," *Bulletin of the American Physical Society*, Vol. 32, No. 2079, 1987, p. 590.

[67] Gaster, M., "On the Effects of Boundary-Layer Growth on Flow Stability," *Journal of Fluid Mechanics*, Vol. 66, No. 3, 1974, pp. 465–480.
https://doi.org/10.1017/S0022112074000310

[68] Herbert, T., "Parabolized Stability Equations," *Annual Review of Fluid Mechanics*, Vol. 29, No. 1, 1997, pp. 245–283.
https://doi.org/10.1146/annurev.fluid.29.1.245

[69] Chang, C.-L., Malik, M., Erlebacher, G., and Hussaini, M., "Compressible Stability of Growing Boundary Layers Using Parabolized Stability Equations," *22nd Fluid Dynamics, Plasma Dynamics and Lasers Conference*, AIAA Paper 1991-1636, 1991.
https://doi.org/10.2514/6.1991-1636

[70] Li, F., and Malik, M. R., "On the Nature of PSE Approximation," *Theoretical and Computational Fluid Dynamics*, Vol. 8, No. 4, 1996, pp. 253–273.
https://doi.org/10.1007/BF00639695

[71] Browne, O. M. F., Haas, A. P., Fasel, H. F., and Brehm, C., "An Efficient Linear Wavepacket Tracking Method for Hypersonic Boundary-Layer Stability Prediction," *Journal of Computational Physics*, Vol. 380, March 2019, pp. 243–268.
https://doi.org/10.1016/j.jcp.2018.11.028

[72] Browne, O. M. F., Haas, A. P., Fasel, H. F., and Brehm, C., "An Efficient Strategy for Computing Wave-Packets in High-Speed Boundary Layers," *47th AIAA Fluid Dynamics Conference*, AIAA Paper 2017-3636, 2017.
https://doi.org/10.2514/6.2017-3636

[73] Browne, O. M., Haas, A. P., Fasel, H. F., and Brehm, C., "A Nonlinear Compressible Flow Disturbance Formulation for Adaptive Mesh Refinement Wavepacket Tracking in Hypersonic Boundary-Layer Flows," *Computers & Fluids*, Vol. 240, May 2022, Paper 105395.
https://doi.org/10.1016/j.compfluid.2022.105395

[74] Balay, S., Abhyankar, S., Adams, M. F., Benson, S., Brown, J., Brune, P., Buschelman, K., Constantinescu, E. M., Dalcin, L., Dener, A., et al., "PETSc Web Page," 2024, https://petsc.org/-https://petsc.org/.

[75] Haas, A. P., Browne, O. M., Fasel, H. F., and Brehm, C., "A Time-Spectral Approximate Jacobian Based Linearized Compressible Navier-Stokes Solver for High-Speed Boundary-Layer Receptivity and Stability," *Journal of Computational Physics*, Vol. 405, March 2020, Paper 108978.
https://doi.org/10.1016/j.jcp.2019.108978

[76] Park, C., *Nonequilibrium Hypersonic Aerothermodynamics*, 1st ed., Wiley, New York, 1990.

[77] Park, C., "A Review of Reaction Rates in High Temperature Air," *24th Thermophysics Conference*, AIAA Paper 1989-1740, 1989.
https://doi.org/10.2514/6.1989-1740

[78] Hameed, A., "Spectral Analysis of Hypersonic Boundary-Layer Instability," Ph.D. Thesis, Stevens Inst. of Technology, Hoboken, NJ, 2023.

[79] Girard, J., Finch, P. M., Schwartz, T., Yu, W. M., Strand, C. L., Austin, J. M., Hornung, H. G., and Hanson, R. K., "Characterization of the T5 Reflected Shock Tunnel Freestream Temperature, Velocity, and Composition Using Laser Absorption Spectroscopy," *AIAA Propulsion and Energy 2021 Forum*, AIAA Paper 2021-3525, 2021.
https://doi.org/10.2514/6.2021-3525

M. Choudhari
Associate Editor